Theoret. Comput. Fluid Dynamics (2004) 18: 197–204
Digital Object Identifier (DOI) 10.1007/s00162-004-0125-5

Theoretical and Computational Fluid Dynamics

Original article

Instabilities of the Stewartson layer Part 2. Supercritical mode transitions

Rainer Hollerbach*, Birgit Futterer, Tamar More**, Christoph Egbers

Department of Aerodynamics and Fluid Mechanics, Brandenburg Technical University, 03013 Cottbus, Germany

Received September 3, 2003 / Accepted May 25, 2004
Published online September 1, 2004 – © Springer-Verlag 2004
Communicated by H.J.S. Fernando

Abstract. We investigate, both experimentally and numerically, the fluid flow in a spherical shell with radius ratio $r_i/r_o = 2/3$. Both spheres rotate about a common axis, with $\Omega_i > \Omega_o$. The basic state consists of a Stewartson layer situated on the tangent cylinder, the cylinder parallel to the axis of rotation and touching the inner sphere. If the differential rotation is sufficiently large, non-axisymmetric instabilities arise, with the wavenumber of the most unstable mode increasing with increasing overall rotation. In the increasingly supercritical regime, a series of mode transitions occurs in which the wavenumber decreases again. The experimental and numerical results are in good agreement regarding this basic sequence of mode transitions, and the numerics are then used to study some of the finer details of the solutions that could not be observed in the experiment.

Key words: spherical Couette flow, hydrodynamic stability, shear layers

1 Introduction

In the classical Taylor–Couette problem of the flow between differentially rotating cylinders or spheres, the differential rotation $(\Omega_i - \Omega_o)$ is typically bigger than the average rotation $(\Omega_i + \Omega_o)/2$, with $\Omega_o = 0$ (and hence $\Delta\Omega = 2\Omega_{av}$) being the simplest, textbook example. In this work we will consider instead the limit where the overall rotation is large, and the differential rotation relatively small. Aside from being an interesting variant on the classical Taylor–Couette problem, this limit is also of considerable interest in geophysical fluid dynamics such as meteorology or oceanography, in which a rapid overall rotation is typically a dominant feature. Here too we will find that the presence of an overall rotation radically alters the behaviour from that found in the classical problem.

Consider then a spherical shell in rapid overall rotation Ω, with additionally a differential rotation $\Delta\Omega$ imposed on the inner sphere. Scaling length by the gap width $(r_o - r_i)$, time by the inverse rotation rate Ω^{-1},

Correspondence to: R. Hollerbach (e-mail: rh@maths.gla.ac.uk)
* *Permanent address:* Department of Mathematics, University of Glasgow, Glasgow, G12 8QW, UK
** *Permanent address:* Department of Physics and Chemistry, University of Portland, Portland, OR 97203, USA

and $\mathbf{U}$ by $\Delta\Omega(r_o - r_i)$, the Navier–Stokes equation in the rotating frame becomes

$$\frac{\partial}{\partial t}\mathbf{U} + Ro\,\mathbf{U}\cdot\nabla\mathbf{U} + 2\,\hat{\mathbf{e}}_z \times \mathbf{U} = -\nabla p + E\,\nabla^2\mathbf{U}, \tag{1}$$

where the Ekman and Rossby numbers

$$E = \frac{\nu}{\Omega(r_o - r_i)^2} \qquad \text{and} \qquad Ro = \frac{\Delta\Omega}{\Omega} \tag{2}$$

measure the overall and differential rotation rates, respectively. The associated boundary conditions are the usual spherical Couette flow boundary conditions

$$\mathbf{U} = r_i \sin\theta\,\hat{\mathbf{e}}_\phi \quad \text{at} \quad r = r_i, \qquad\qquad \mathbf{U} = 0 \quad \text{at} \quad r = r_o. \tag{3}$$

In a previous paper (Hollerbach [8], hereafter referred to as I) we numerically solved (1–3), for the particular radius ratio $r_i/r_o = 1/3$. We began by considering the axisymmetric basic state and showed how an increasingly rapid overall rotation leads to the formation of a Stewartson layer on the tangent cylinder, the cylinder just touching the inner sphere and parallel to the axis of rotation. We then considered the non-axisymmetric instabilities that arise for sufficiently large differential rotation rates, and found them to be very different for positive versus negative Ro, with positive Ro yielding a progression to higher and higher azimuthal wavenumbers m for an increasingly rapid overall rotation, but negative Ro yielding only $m = 1$.

In this paper we will again consider this problem defined by (1–3), but now experimentally as well as numerically, using the apparatus described by Egbers and Rath [4]. Very briefly, it consists of concentric spheres of radii $r_i = 26.7$ mm and $r_o = 40.0$ mm, which can be independently rotated about a common axis at speeds up to 300 rev/min. The fluid filling the gap is Bayer Baysilone® M3 silicone oil, having a viscosity of ~3.3 cSt. At Ekman numbers as small as $10^{-3.1}$ we could thus still reach Rossby numbers as large as 0.6. This value of E is not nearly as small as the 10^{-5} considered in I, but turned out to be small enough to obtain a reasonably well-defined Stewartson layer (see Fig. 1 below).

As in I, we then turn our attention to these non-axisymmetric instabilities (although for positive Ro only this time). Very conveniently, we find that this progression to higher m noted above seems to occur much quicker in the thinner gap considered here, so that by $E = 10^{-3.1}$ we are already up to $m = 6$. Finally, going beyond the linear onset calculations presented in I, we also explore the nonlinear equilibration of these instabilities, and find that in the increasingly supercritical regime the system switches back to progressively lower m, with good agreement between numerical and experimental results for both the linear onset as well as these supercritical transitions.

2 The basic state

Figure 1 shows the numerically computed solutions at $Ro = 0$, corresponding to an infinitesimal differential rotation, and $E = 10^{-2.5}$, $10^{-2.8}$ and $10^{-3.1}$, corresponding to an increasingly rapid overall rotation. Focusing on the angular velocity ω, we see very clearly the emergence of an increasingly thin shear layer, the so-called Stewartson layer, on the tangent cylinder $\mathcal{C}$, with $\omega \approx 1/2$ inside $\mathcal{C}$ but zero outside. In order to understand why the solutions should arrange themselves in this peculiar fashion, we recall the Taylor–Proudman theorem, stating that in rapidly rotating systems the flow will tend to align itself along the axis of rotation. More formally, taking the curl of Eq. (1) and using ∂_t, Ro, $E \ll 1$ (in fact ∂_t and Ro are zero in Fig. 1), we obtain $\partial\mathbf{U}/\partial z \approx 0$. With this result, these solutions in Fig. 1 follow quite naturally: For fluid columns outside $\mathcal{C}$, $\omega = 0$ is the boundary condition at both the upper and lower boundaries, so $\omega = 0$ everywhere along the column will satisfy both the Taylor–Proudman theorem as well as the boundary conditions. In contrast, for fluid columns inside $\mathcal{C}$, $\omega = 0$ is still the upper boundary condition, but the lower boundary condition is now $\omega = 1$. It is therefore not possible to satisfy the Taylor–Proudman theorem everywhere along the column. Instead, it is satisfied in the interior by having $\omega \approx 1/2$, with all the necessary z-dependence concentrated in the so-called Ekman layers at the top and bottom boundaries.

The purpose of the Stewartson layer therefore is to resolve this jump in ω across $\mathcal{C}$. Stewartson [9] showed its detailed structure to consist of nested layers of innermost thickness $E^{1/3}$ right on $\mathcal{C}$, and outer

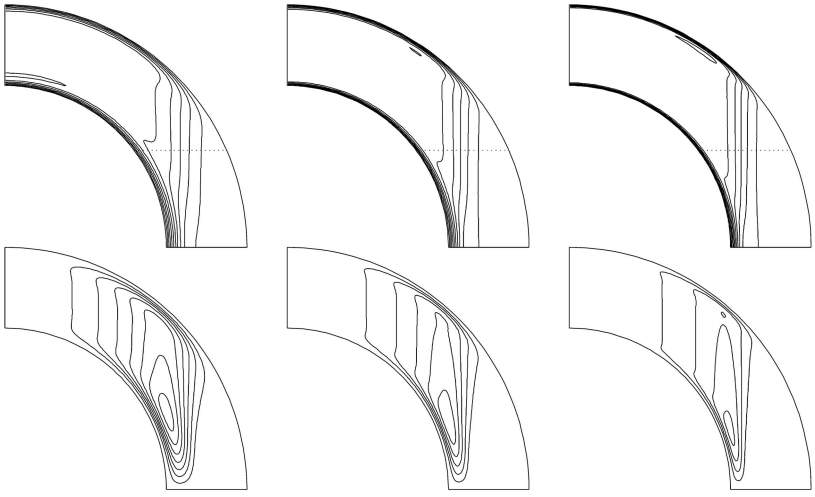

Fig. 1. The top row shows contour plots of the angular velocity ω. From left to right $E = 10^{-2.5}$, $10^{-2.8}$ and $10^{-3.1}$, and all three at $Ro = 0$. The bottom row shows the associated meridional circulation. This circulation is very weak though, only $O(E^{1/2})$, and therefore plays no important role in the dynamics. The angular velocity is symmetric about the equator, the meridional circulation antisymmetric (that is, counter-clockwise in the upper hemisphere, clockwise in the lower). The contour intervals are 1/11 for the top row, 0.01 for the bottom. Finally, the dotted lines in the top row indicate the planes $z = 1.2$; in Fig. 2 we show profiles of ω along these lines

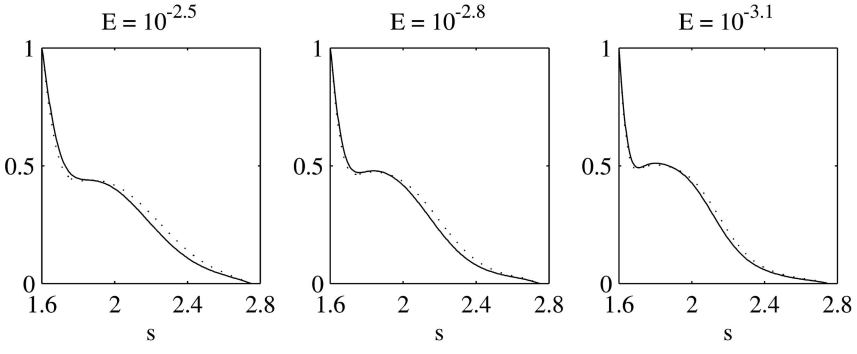

Fig. 2. Profiles of ω as a function of cylindrical radius s, at $z = 1.2$. The solid lines are for $Ro = 0$, as in Fig. 1. The dashed lines are for $Ro = 0.4$, 0.3 and 0.2, for $E = 10^{-2.5}$, $10^{-2.8}$ and $10^{-3.1}$, respectively. As one can see in Fig. 3, these values are still slightly below the linear stability boundary

thicknesses $E^{2/7}$ just inside $\mathcal{C}$ and $E^{1/4}$ just outside. The Ekman layers scale as $E^{1/2}$, except near the equator of the inner sphere, where they scale as $E^{2/5}$. The results in Fig. 1 are broadly consistent with these scalings (for example, the inner Ekman layers are noticeably thicker near the equator), even if the range in E is not sufficient to distinguish these various sublayers. See, however, Hollerbach [6] or Dormy et al. [2] for more thorough comparisons of numerical results with Stewartson's asymptotics.

Figure 2 shows detailed profiles of ω across the Stewartson layer, showing ω as a function of the cylindrical radius s, at the particular height $z = 1.2$ (where we remember that with our nondimensionalization $r_i = 2$ and $r_o = 3$). We see very clearly the Ekman layer at the inner boundary $s = 1.6$ (at this particular value of z), and the Stewartson layer at the tangent cylinder $s = 2$. One point to note, both here and in Fig. 1, is that while the Stewartson layer is somewhat more crowded in this case than in the wider gap considered in I, this range $E = 10^{-2.5}$–$10^{-3.1}$ is sufficiently small for it to be reasonably well-developed, and distinct from the Ekman layers.

3 Instabilities

All of these results so far are for infinitesimal differential rotation $Ro = 0$. The next question therefore is what happens for finite differential rotation? The axisymmetric basic states in fact change remarkably

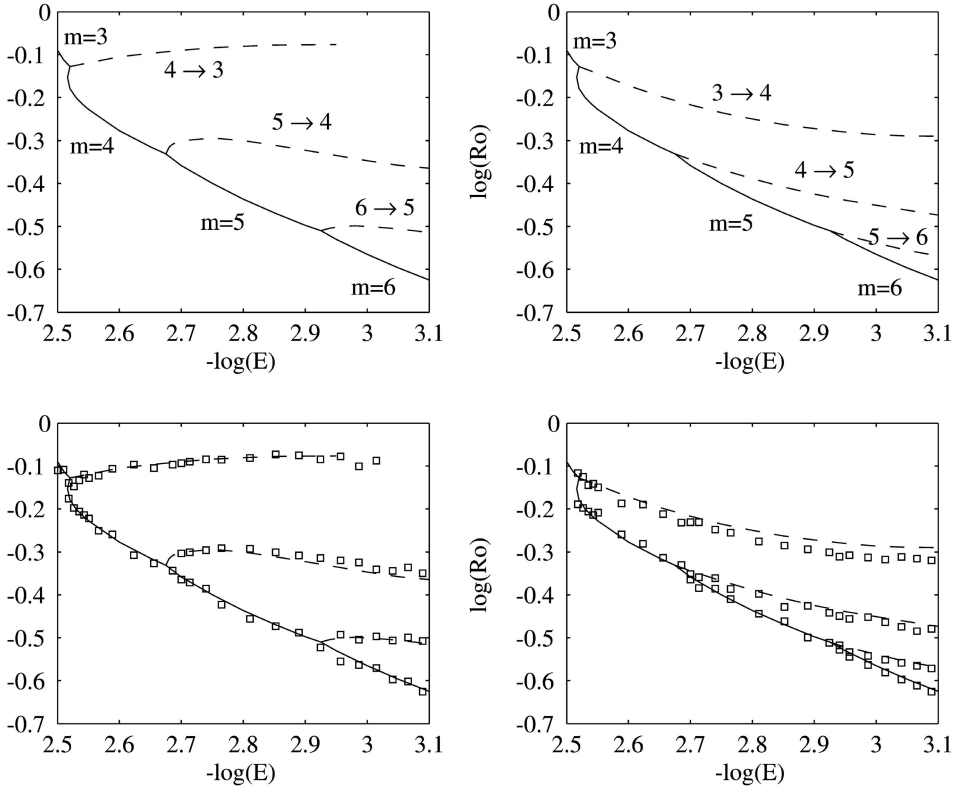

Fig. 3. The solid lines labelled $m = 3, 4, 5, 6$ in either of the top two panels are the numerically computed linear onset curves of the indicated modes. The dashed lines labelled '$m \to m-1$' in the top left panel are the transitions obtained when increasing *Ro*, the dashed lines labelled '$m \to m+1$' in the top right panel the reverse transitions obtained when decreasing *Ro* again. In the bottom two panels the corresponding transitions observed in the experiment have been plotted on top of the numerical results. Finally, the last portion of the $4 \to 3$ transition could not be reached either experimentally or numerically. In the experiment this would have required greater Ω_i than could be achieved, in the numerics greater truncations than could be achieved. (Truncations up to 50 Chebyshev modes in r, and spherical harmonics up to $l = 180$, $m = 48$ were used. See also Hollerbach [7] for the details of the numerical method.)

little, with Fig. 2 showing profiles for non-zero *Ro* as well. However, for sufficiently large differential rotation it seems inevitable that some sort of instability will set in, by a mechanism similar to the classical Kelvin–Helmholtz instability. That is, we would expect the initially axisymmetric Stewartson layer to develop a non-axisymmetric, wavy structure instead. In I we computed the linear onset of these instabilities, and explored the origin of this difference between positive and negative *Ro* noted above. See also Busse [1] for an asymptotic analysis of this linear onset problem (but in a cylindrical geometry in which this difference between positive and negative *Ro* does *not* arise).

In this work we restrict attention to positive *Ro*, but now go beyond just the linear onset, and explore the nonlinear equilibration as well. Figure 3 summarizes the essence of this whole paper. The solid lines in either of the top two panels denote the numerically computed linear onset curves. With decreasing E we obtain the same progression to higher m found in I, and very conveniently it seems to happen quicker in this case, with $E = 10^{-3.1}$ being sufficient to reach $m = 6$ (as opposed to $10^{-4.6}$ in I). The other interesting point to note here is the transition from $m = 3$ to 4, which is slightly different from the others; whereas the other transitions are simple mode crossings, the one from 3 to 4 involves the $m = 4$ curve turning back on itself so that its upper part crosses the $m = 3$ curve. This means that the minimum Rossby number needed for instability decreases abruptly in going from 3 to 4, rather than varying continuously as for all the other transitions.

Figure 3 also shows the nonlinear equilibration in the supercritical regime. Suppose, for example, that we fix $E = 10^{-3.1}$ and gradually increase *Ro*. According to the linear onset curves, the most unstable mode is then $m = 6$, with $Ro_c = 0.237$. In the slightly supercritical regime, we would therefore expect the in-

stability to equilibrate at some finite amplitude, and to contain only multiples of this basic wavenumber $m_0 = 6$. This is exactly what was observed up to $Ro = 0.306$. Beyond that value, however, this $m_0 = 6$ solution is unstable, and the system switches instead to an $m_0 = 5$ solution. Increasing Ro further, at 0.432 this in turn yields to $m_0 = 4$, and so on down to $m_0 = 3$. The top left panel in Fig. 3 shows how the critical Rossby numbers for these supercritical mode transitions vary with E. Finally, if one then decreases Ro again, one obtains the whole sequence in reverse, but with a considerable degree of hysteresis, as seen in the top right panel.

Turning next to the experimental results, these are shown in the bottom two panels in Fig. 3, in each case superimposed on the corresponding numerical results for either increasing or decreasing Ro. The experimental procedure was to fix Ω_o (that is, E), then adjust Ω_i in steps of 1 rpm, corresponding to 2–3% in Ro. After each increment 10–15 minutes were allowed to pass, corresponding to several hundred times the spin-up timescale $(r_o - r_i)/(\nu\Omega_o)^{1/2}$ (e.g., Duck and Foster [3]). If no mode transition had occurred in that time, Ω_i was changed again, and so on. Comparing these results with the numerical ones, we see that the agreement is very good. There is no need even to label which particular transition a given square corresponds to; they are all sufficiently close to the numerical results that the correspondence is obvious. The size of the squares also gives some indication of the measurement error; the errors in $\log(E)$ and $\log(Ro)$ were both around 0.01–0.02 (due primarily to temperature-induced variations in viscosity for $\log(E)$, and to the necessarily finite increments in which Ω_i was adjusted for $\log(Ro)$).

It is worth noting also that Früh and Read [5] obtained similar results in a similar experiment in cylindrical geometry. They too obtained a progression to higher wavenumbers with decreasing E, and then transitions back to lower m with increasing Ro. However, there are also differences between the two experiments: some of their solutions fluctuated in time, whereas ours are steady, merely drifting in longitude. The cause of this difference is not known, but the difference in spherical versus cylindrical geometry alone may be quite important (see also I).

4 Spatial structures

Having obtained this agreement between experimental and numerical results, the next question we would like to address is what these solutions actually look like. Figure 4 summarizes these results. The top row shows the streamfunction of the vertically integrated horizontal flow. That is, if $\mathbf{U} = (U_z, U_s, U_\phi)$, consider $\mathbf{V}_H = (0, \int U_s\, dz, \int U_\phi\, dz)$. By construction this flow is independent of z, so it has a streamfunction representation. Also, since the original $\mathbf{U}$ is almost independent of z (see below) $\mathbf{V}_H$ will indeed be the dominant part of the flow. Showing its streamfunction is therefore the most compact way of representing the essential features of the solution. And as expected, the originally circular Stewartson layer is distorted first into a hexagon, then a pentagon, a square, and ultimately the triangular $m_0 = 3$ mode, just as indicated in Fig. 3. The other interesting feature to note in these plots is how most of the distortion occurs outside the tangent cylinder; the streamlines inside $\mathcal{C}$ remain relatively circular.

As noted above, this z-integrated horizontal flow $\mathbf{V}_H$ is by far the dominant part of the flow (accounting for over 90% of the total kinetic energy, for example). We would nevertheless like to have some idea of what the z-component of the flow looks like as well. In particular, if fluid columns are moving in and out in s, as we just saw in the first row, and if the height of these columns varies in s, as the underlying geometry forces them to, then the flow must necessarily also have a z-component. The second row in Fig. 4, therefore, shows contour plots of U_z in this same $z = 1.2$ plane previously introduced in Fig. 2. And indeed, there is a certain up and down motion as well, again concentrated in the vicinity of the tangent cylinder.

The third row in Fig. 4 shows the axisymmetric part of the angular velocity. The two points to note here are, first, the flow does indeed continue to be largely independent of z, even for the $m_0 = 3$ mode, at roughly 2.5 times Ro_c. Second, while decreasing E makes the Stewartson layer thinner (as shown in Figs. 1 and 2), increasing Ro broadens it again. That is, the effect of these non-axisymmetric instabilities seems to be to suppress the shear that spawned them in the first place. In Fig. 5 we will also consider this influence of the instabilities back on the basic state in more quantitative detail.

Finally, the last row in Fig. 4 shows photographs of the experiment. The agreement with the top row is excellent. The only difference is that the corners seem to be somewhat sharper here than in $\mathbf{V}_H$. Given the qualitative nature of the visualization technique (aluminium flakes suspended in the fluid) it is unfortunately

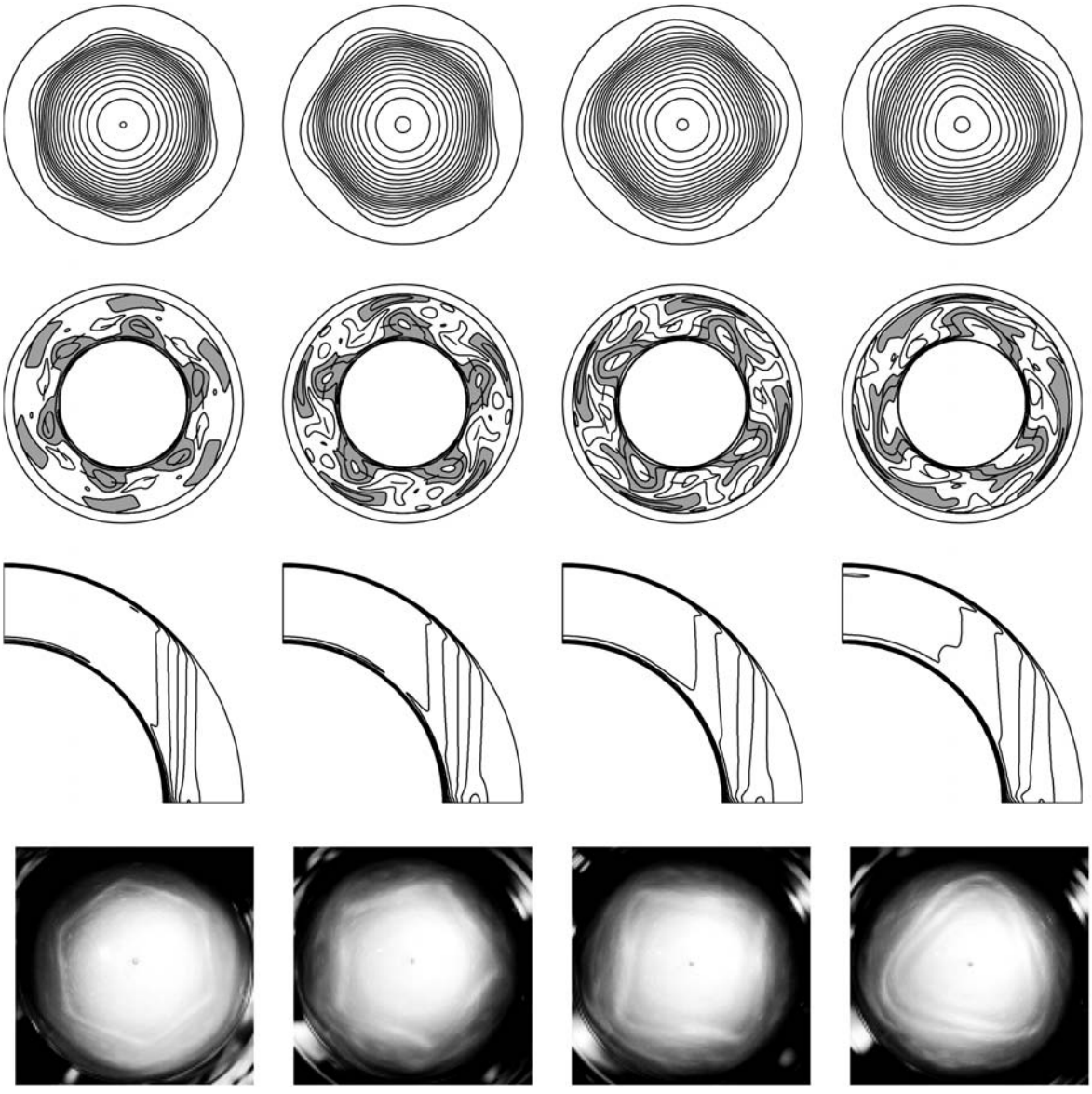

Fig. 4. As noted in the text, the top row shows streamlines of the z-integrated horizontal flow $\mathbf{V}_H$, the second row shows contours of U_z in the plane $z = 1.2$, with negative contours shaded, and the third row shows contours of the axisymmetric part of the angular velocity U_ϕ/s. The contour intervals are 0.1, 0.1 and $1/11$, respectively. In the top two rows the outer circle is the outer boundary $s = 3$. The other circles in the second row are at $s = 1.6$ and 2.75, where the plane $z = 1.2$ intersects the spherical shell, and (dashed) at the tangent cylinder location $s = 2$. From left to right $Ro = 0.3$, 0.4, 0.5 and 0.6, and all four at $E = 10^{-3.1}$. The longitudinal drift rates of these modes are 0.083Ω, 0.101Ω, 0.113Ω and 0.115Ω for $m_0 = 6$, 5, 4 and 3, respectively. The last row shows photographs of the experiment, looking straight down from above, and at these same parameter values $Ro = 0.3$, 0.4, 0.5 and 0.6, and $E = 10^{-3.1}$

not clear how closely the two figures should match, so it's difficult to assess the significance of this slight discrepancy. Further details such as U_z or ω could also not be obtained with this visualization technique, but in view of this general agreement in $\mathbf{V}_H$ that is hardly necessary. We are clearly observing the same solutions in both cases, and the visualization was certainly more than adequate to allow a determination of the mode number, which is all that is required to obtain the results in Fig. 3.

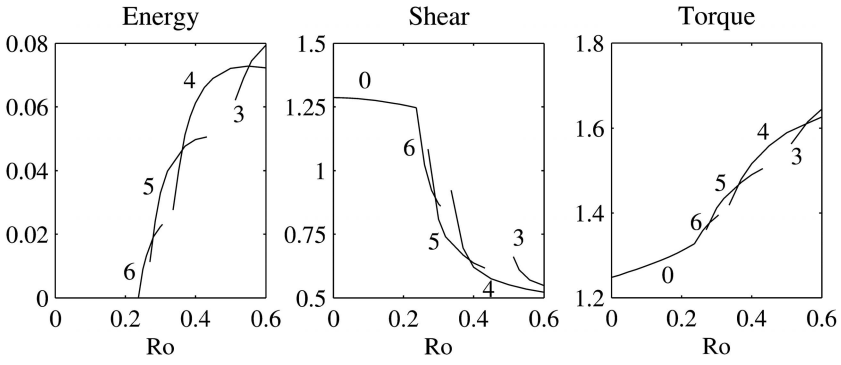

Fig. 5. As noted in the text, the first panel shows the fraction of the kinetic energy contained in the non-axisymmetric modes, the second panel shows the maximum shear in the Stewartson layer, and the last panel shows the torque on the inner sphere. $E = 10^{-3.1}$, and Ro increases from 0 to 0.6. The different mode numbers are indicated by each curve, with 0 denoting the purely axisymmetric basic state, before the onset of any instabilities

5 Diagnostics

We conclude with various diagnostic quantities, including this shear-suppressing back-reaction alluded to above. The first panel in Fig. 5 shows the fraction of the total kinetic energy contained in the non-axisymmetric modes. This is thus a simple measure of the amplitude at which the instabilities equilibrate, and shows that the flow continues to be dominated by the basic state (as is also evident in the $\mathbf{V}_H$ plots in Fig. 4).

The second panel shows the maximum shear in the Stewartson layer. More precisely, fix $z = 1.2$ and consider ω as a function of s (as in Fig. 2). Then compute $d\omega/ds$, and find its maximum value (outside the Ekman layer, so restricting attention to $s > 1.8$, say). It is this quantity $|d\omega/ds|_{\max}$ that is plotted in this second panel, and the results are quite revealing indeed. In particular, we note that as long as the solution remains axisymmetric, that is, in the range $0 \le Ro \le 0.237$, the maximum shear hardly varies with Ro. As soon as the non-axisymmetric instabilities set in though, they dramatically suppress the shear; despite the fact that the $m_0 = 6$ mode never amounts to much more than 2% of the total kinetic energy, it alone already suppresses the shear by roughly a third, with the more strongly supercritical $m_0 = 5$, 4 and 3 modes suppressing it further still. This is therefore the quantitative version of this shear-suppression previously noted in Fig. 4.

The third panel shows the torque

$$T = E \int r^2 \frac{\partial}{\partial r}\Big(\frac{U_\phi}{r}\Big) \sin\theta \, dS \tag{4}$$

one must exert on the inner sphere to maintain its differential rotation. Just as with the shear, the torque too changes more strongly in the non-axisymmetric than in the axisymmetric regime, but the effect is not as pronounced. We can perhaps begin to understand why by noting that in a steady-state, the work done by this torque must exactly balance the viscous dissipation throughout the fluid (as indeed it did, to within better than 0.1%). By generating structures in ϕ where previously there were none, the onset of instability might therefore be expected to increase the dissipation, and hence the required torque. On the other hand, this shear-suppression noted above tends to reduce the structure in s, and hence the dissipation and torque. It is the competition between these two effects which presumably explains why the torque does not change as dramatically as the shear.

Finally, these various diagnostics might perhaps give some idea of *why* these mode transitions occur at all. One explanation might be that it is due to this shear-suppression; as the instabilities broaden the Stewartson layer again, the preferred azimuthal wavenumber decreases, just as in the linear onset problem broader Stewartson layers (larger E) correspond to smaller m. This is unlikely to be the complete answer though, for the following reason: We note in Fig. 5 that over most of the range, two or even three modes can have the same shear. If a given shear uniquely determined the wavenumber, however, as the argument above suggests, this clearly could not happen.

Another possibility might be that the system seeks to maximize its viscous dissipation. We note, for example, that the torque increases at every mode transition, for both increasing and decreasing *Ro* (as is also the case for the kinetic energy fraction). One could imagine, therefore, a 'competition' among the different mode numbers, with the one capable of achieving the greatest amplitude and dissipation at that given Rossby number winning out, and only yielding to a larger or smaller m_0 when that mode becomes more efficient. Both of these explanations are qualitative at best though, so we conclude by noting that there are aspects of this problem that are still not fully understood.

Acknowledgments. RH's visit in Germany was supported by the Alexander von Humboldt Foundation, TM's by the German Academic Exchange Service (DAAD). BF is supported by DLR grant 55-WM-0122. The silicone oil was kindly donated by Bayer.

References

1. Busse, F.H.: Shear flow instabilities in rotating systems. J. Fluid Mech. **33**, 577–589 (1968)
2. Dormy, E., Cardin, P., Jault, D.: MHD flow in a slightly differentially rotating spherical shell, with a conducting inner core, in a dipolar magnetic field. Earth Planet. Sci. Lett. **160**, 15–30 (1998)
3. Duck, P.W., Foster, M.R.: Spin-up of homogeneous and stratified fluids. Ann. Rev. Fluid Mech. **33**, 231–263 (2001).
4. Egbers, C., Rath, H.J.: The existence of Taylor vortices and wide-gap instabilities in spherical Couette flow. Acta Mech. **111**, 125–140 (1995).
5. Früh, W.G., Read, P.L.: Experiments on a barotropic rotating shear layer. Part 1. Instability and steady vortices. J. Fluid Mech. **383**, 143–173 (1999)
6. Hollerbach, R.: Magnetohydrodynamic Ekman and Stewartson layers in a rotating spherical shell. Proc. R. Soc. Lond. A **444**, 333–346 (1994)
7. Hollerbach, R.: A spectral solution of the magneto-convection equations in spherical geometry. Int. J. Numer. Meth. Fluids **32**, 773–797 (2000)
8. Hollerbach, R.: Instabilities of the Stewartson layer. Part 1. The dependence on the sign of *Ro*. J. Fluid Mech. **492**, 289–302 (2003)
9. Stewartson, K.: On almost rigid rotations. Part 2. J. Fluid Mech. **26**, 131–144 (1966)